Engineering Fracture Mechanics 78 (2011) 301–316

Contents lists available at ScienceDirect

Engineering Fracture Mechanics

journal homepage: www.elsevier.com/locate/engfracmech

An element enriched formulation for simulation of splitting failure

D. Dias-da-Costa [a,*], J. Veludo [b], J. Alfaiate [c], E. Júlio [a,1]

[a] ISISE, Civil Eng. Dept., University of Coimbra, Rua Luís Reis Santos, 3030-788 Coimbra, Portugal
[b] ISISE, Polytechnic Institute of Leiria, Campus 2, Morro do Lena – Alto do Vieiro, Apartado 4163, 2411-901 Leiria, Portugal
[c] IST and ICIST, Civil Eng. Dept., Instituto Superior Técnico, Av. Rovisco Pais, 1049-001 Lisboa, Portugal

ARTICLE INFO

Article history:
Received 19 May 2010
Received in revised form 1 September 2010
Accepted 9 September 2010
Available online 29 September 2010

Keywords:
Radial splitting
Discrete discontinuities
Axisymmetric model
Strong discontinuity

ABSTRACT

Radial cracking propagation is often related to the bond transfer mechanism induced by slippage of a deformed bar. However, this failure pattern can also develop in other situations, namely: (*i*) concrete pipes submitted to an excessive inner pressure or (*ii*) concrete structures exposed to adverse environmental conditions under which corrosion or frost develops.

In this paper a new contribution for the simulation of radial splitting failure is given. A discrete strong discontinuity formulation is presented which is fully capable of embedding radial discontinuities into axisymmetric finite elements. Numerical examples are used to show: (*i*) the capability of fully softening the applied inner pressure and (*ii*) mesh independence. Comparison with two published analytical approaches is performed for varying brittleness numbers. Finally, the model is applied to the simulation of both plain and reinforced concrete cylinders subjected to increasing inner pressure. A good agreement with experimental data is obtained.

1. Introduction

Radial splitting failure mechanism appears in numerous situations. Some examples are: (*i*) concrete pipes submitted to excessive inner pressure; (*ii*) concrete structures exposed to adverse environmental conditions with development of corrosion or frost; or (*iii*) the bond transfer mechanism between reinforcement bars and surrounding concrete. Concerning the latter, it is currently assumed that three main mechanisms contribute to the composite behaviour of the connection: (*i*) chemical adhesion; (*ii*) friction; and (*iii*) mechanical interaction. Usually, one (or two) mechanisms can prevail over the other(s). For instance, for smooth bars, chemical adhesion and friction are crucial, whereas for ribbed bars, mechanical interaction is the most significant. For ribbed bars, friction is only important after a significant slip occurs with respect to the concrete which crushes in front of the ribs [1]. In fact, such slip magnitude induces transverse and longitudinal cracking. The ribs of the deformed bar induce bearing stresses in the surrounding concrete, forming a conical strut-tie system, which develops along the bar. The tangential component is called bond stress, whereas the radial component applies a confining pressure to the bar. The development of bond stresses induces tensile hoop stresses, which can exceed the ultimate tensile stress with consequent propagation of longitudinal cracks and wedging (Fig. 1).

The radial component of the bond can be compared to a hydraulic pressure, acting on a thick-walled concrete ring, balanced by hoop tensile stresses in concrete [1] (Fig. 1). Therefore, the study of the behaviour of concrete covers for reinforcement bars is frequently based on models developed for that kind of problems. Some fundamental aspects are:

---

[*] Corresponding author. Tel.: +351 239797256; fax: +351 239797259.
E-mail addresses: dcosta@dec.uc.pt (D. Dias-da-Costa), joao.veludo@ipleiria.pt (J. Veludo), alfaiate@civil.ist.utl.pt (J. Alfaiate), ejulio@dec.uc.pt (E. Júlio).
[1] Tel.: +351 239797256; fax: +351 239797259.

0013-7944/$ - see front matter © 2010 Elsevier Ltd. All rights reserved.
doi:10.1016/j.engfracmech.2010.09.010

Nomenclature

$\mathbf{a}$	total displacement vector at the nodes
$\hat{\mathbf{a}}$	regular displacement vector at the nodes
$\tilde{\mathbf{a}}$	enhanced displacement vector at the nodes
$\bar{\mathbf{b}}$	body forces vector
B	parameter
$\mathbf{B}$	strain-nodal displacement matrix
d	scalar damage
$\mathbf{D}$	constitutive matrix
E	Young's modulus
f	loading function
$\hat{\mathbf{f}}$	regular external vector force at the regular nodes
f_{c0}	compressive strength of concrete
f_{sy}	tensile strength of steel
f_{t0}	tensile strength of concrete
$\tilde{f}_\theta$	enhanced external force at the enhanced degree of freedom
G_F	fracture energy
κ	scalar variable depending on the hoop jump component
k_θ	hoop penalty parameter
$\mathbf{K}_{\hat{a}\hat{a}}$	bulk stiffness matrix
$\mathbf{K}_{aw}$, $\mathbf{K}_{wa}$	enhanced stiffness matrices
$\mathbf{K}_{con}$	condensed stiffness matrix
K_d	discontinuity stiffness matrix
l_{ch}	Hillerborg's characteristic length
$\mathbf{M}_w$	jump function matrix
$\mathbf{M}_w^k$	matrix composed by evaluating $\mathbf{M}_w$ at each finite element node
n_d	number of active discontinuities
$\mathbf{N}$	shape function matrix
P_f, P_i	final and initial perimeter, respectively
p_i	internal pressure
p_{max}	maximum internal pressure
R	radius
$\mathbf{T}$	discontinuity constitutive matrix
$\mathbf{t}_\theta$	traction vector
$\bar{\mathbf{t}}$	natural forces vector
$\mathbf{u}$	total displacement vector
$\bar{\mathbf{u}}$	essential boundary conditions vector
$\hat{\mathbf{u}}$	regular displacement field vector
$\tilde{\mathbf{u}}$	enhanced displacement field vector
$[\mathbf{u}]$	jump vector
U_r	normalised radial displacement
Ω	elastic domain
Γ	boundary
Γ_d	discontinuity's surface
Γ_t	boundary with natural forces
Γ_u	boundary with essential conditions
w_θ	nodal hoop jump
$\mathbf{x} = (x_r, x_z, x_\theta)$	global coordinates of a material point
$\boldsymbol{\varepsilon}$	total strain tensor
$\hat{\boldsymbol{\varepsilon}}$	regular strain tensor
$\boldsymbol{\sigma}$	stress tensor
ν	Poisson ratio
$d(\cdot)$	incremental variation of $(\cdot)$
$(\cdot)^s$	symmetric part of $(\cdot)$
$\delta(\cdot)$	admissible or virtual variation of $(\cdot)$
$(\cdot)^e$	$(\cdot)$ belonging to the finite element e
$(\cdot)_\theta$, $(\cdot)_r$	circumferential and radial components of $(\cdot)$
$\langle\cdot\rangle^+$	McAuley brackets

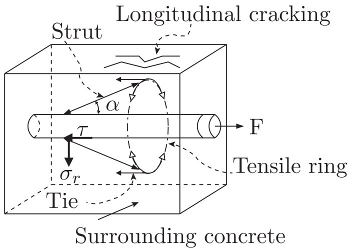

Fig. 1. Bond behaviour of deformed bars: radial component, σ_r, balanced by tensile stresses in the uncracked ring of concrete.

(*i*) the choice of the softening model; (*ii*) the approximation of the displacement field; and (*iii*) the number of active splitting cracks [2]. Under some simplifications, closed-form solutions exist for the stress state in a ring [1,3,4]. These simplifications usually consist of: (*i*) neglecting Poisson's effect for the hoop strain [3] and (*ii*) taking the bond stress equal to the internal pressure. As a consequence of the latter assumption, a similar response under compressive and tensile stresses is adopted for both strut and tie components.

The transfer mechanism of bond involves fracture in three-dimensions in which different failure patterns can develop, namely: conical and radial splitting cracks; and sliding at the interface [5]. Analytical models dealing with splitting cracks have been developed [1,3,4]. Noghabai [4,6] compared a discrete crack model, a smeared crack model and finite elements with inner softening band in the simulation of thick-walled concrete rings under plain strain conditions. A major drawback of these models is the impossibility of considering the different behaviour along the reinforcement and the corresponding sliding at the interface. Few approaches deal with combined sliding and splitting mechanisms [7,8] and usually these are mainly focused on the interface behaviour, assuming simplifications for radial splitting.

In this paper, a new contribution is given for the numerical simulation of radial splitting failure. A discrete strong discontinuity approach is adopted to embed cohesive longitudinal discontinuities in an axisymmetric body. The corresponding hoop jumps are assumed constant inside each finite element and are transferred to the surrounding elements by rigid body motion. The variational framework leads to a symmetric formulation (for symmetric constitutive laws). Static condensation is adopted, which simplifies the implementation of this technique.

The paper is organised as follows: in Section 2 the kinematics of a strong discontinuity, the variational formulation and the discretised equations are derived. The corresponding implementation issues are addressed in Section 3. The adopted material model are briefly reviewed in Section 4. Some simplified examples are presented in Section 5 in order to expose the kinematics of the formulation. Comparison with two published analytical results is made in Section 6. A simulation of an experimental study performed in [4] concerning plain and reinforced concrete cylinders subjected to inner pressure is presented in Section 7. Finally, the most relevant conclusions are summarised in Section 8.

2. Problem description

Consider the axisymmetric elastic body Ω represented in Fig. 2a. It is assumed that radial microcracking starts developing when the hoop stress reaches the tensile strength of the material. In the discrete crack approach, microcraking is supposed to localise into zero width surfaces, designated strong discontinuities [9,10] (Fig. 2a). At these discontinuities, the displacement field is discontinuous but bounded, whereas the strain field is unbounded. Immediately after the onset of localisation, the

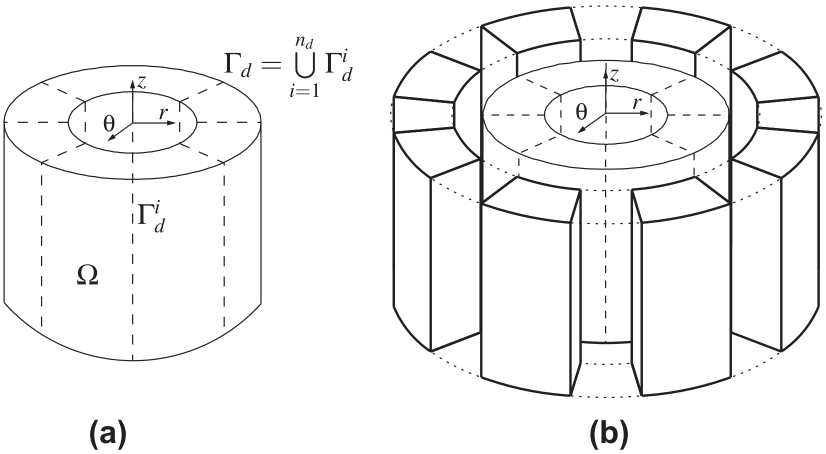

Fig. 2. Domain Ω: (a) localisation into n_d discontinuity surfaces and (b) resultant splitting wedges at a final stage of crack propagation.

behaviour of each discontinuity obeys a stress-jump relationship undergoing softening. Simultaneously, the traction continuity condition enforces gradual unloading of the surrounding bulk. The total displacement of the specimen is the sum of the regular continuous part and the enhanced displacement field, eventually leading to the splitting of the wedges. In Fig. 2b completely separated wedges are represented at a final stage of crack propagation. For clarity, the elastic deformation of the continuum has been neglected.

2.1. Kinematics of a strong discontinuity

Consider that the body Ω, with boundary surface Γ, contains n_d uniformly embedded radial discontinuity surfaces Γ_d^i, such that $\Gamma_d = \bigcup_{i=1}^{n_d} \Gamma_d^i$. Axissimetry around z is assumed for both loading conditions and elastic properties.

The body forces, $\bar{\mathbf{b}}$, are gradually applied to avoid dynamic effects. The natural boundary conditions, $\bar{\mathbf{t}}$, are distributed on the external boundary surface, Γ_t, whereas the essential boundary conditions, $\bar{\mathbf{u}}$, are applied in Γ_u, such that $\Gamma_t \cup \Gamma_u = \Gamma$ and $\Gamma_t \cap \Gamma_u = \emptyset$.

In the bulk, the total displacement, $\mathbf{u}$, is decomposed into the sum of a regular displacement field, $\hat{\mathbf{u}}$, and an enhanced displacement field, $\tilde{\mathbf{u}}$:

$$\mathbf{u}(\mathbf{x}) = \hat{\mathbf{u}}(\mathbf{x}) + \tilde{\mathbf{u}}(\mathbf{x}) \quad \text{in} \quad \Omega \setminus \Gamma_d. \tag{1}$$

Due to axisymmetry, inside each wedge the displacement field is constant along the same hoop. Furthermore, under this condition the jump at each discontinuity must be orthogonal to the discontinuity's surface, therefore parallel to the hoop stress. Regarding the enhanced displacement field a further assumption is made: the work done by the stresses on the enhanced displacement field is null and the stresses in the domain are only due to the regular part of the strain field, i.e.:

$$\boldsymbol{\varepsilon} = \nabla^s \mathbf{u} = \nabla^s \hat{\mathbf{u}} = \hat{\boldsymbol{\varepsilon}} \quad \text{in} \quad \Omega \setminus \Gamma_d. \tag{2}$$

Both displacement and strain fields, represented respectively by Eqs. (1) and (2), are continuous inside each wedge. The study is undertaken in a single plane, (r,z), with z being the axis of axisymmetry.

According to (2) and neglecting the variation of the hoop bulk displacements with respect to the jump displacements, the hoop's final perimeter, P_f, is taken approximately equal the initial bulk perimeter, P_i, plus the hoop jump (Fig. 3):

$$P_f = P_i + n_d[u]_\theta \equiv 2\pi(x_r^i + \tilde{u}_r) = 2\pi x_r^i + n_d[u]_\theta, \tag{3}$$

where $[u]_\theta$ is the jump from each active radial discontinuity, at a certain hoop.

From Eq. (3), the following relation is derived:

$$\tilde{u}_r = \frac{[u]_\theta}{2\pi/n_d}, \tag{4}$$

where $\tilde{u}_r$ is the radial component of the enhanced displacement field.

The number of active discontinuities cannot be evaluated from a bidimensional analysis since it depends on the brittleness of the specimen [5], ranging from several discontinuities, in a ductile material, to one or two for a brittle material. For current specimens, the cracking mechanism is composed by the development of a system of competing active cracks, whereas other cracks in the neighbourhood unload. According to Noghabai [6], for current specimens, two active cracks are usually found contributing to the dissipation of energy.

According to Eq. (4), the enriched displacement in the plane is written as:

$$\tilde{\mathbf{u}} = (\tilde{u}_r, \tilde{u}_z) = \mathbf{M}_w[u]_\theta, \tag{5}$$

with

$$\mathbf{M}_w = \left(\frac{1}{2\pi/n_d}, 0\right). \tag{6}$$

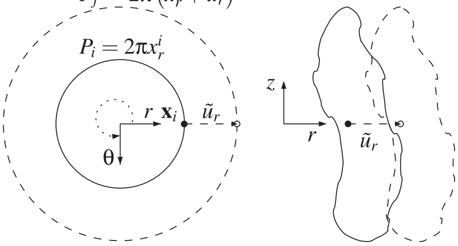

Fig. 3. Enhanced displacement field induced by a discontinuity opening at a material point $\mathbf{X}_i$.

2.2. Variational formulation

The variational formulation for an elastic body crossed by a discontinuity is given by [11]:

$$\int_{\Omega\setminus\Gamma_d} (\nabla^s \delta\mathbf{u}) : \boldsymbol{\sigma}(\boldsymbol{\varepsilon}) d\Omega + \int_{\Gamma_d} \delta[\mathbf{u}] \cdot \mathbf{t}_\theta \, d\Gamma = \int_{\Omega\setminus\Gamma_d} \delta\mathbf{u} \cdot \bar{\mathbf{b}} \, d\Omega + \int_{\Omega_t} \delta\mathbf{u} \cdot \bar{\mathbf{t}} \, d\Omega, \tag{7}$$

where $\delta\mathbf{u}$ are the admissible displacement variations, $\delta[\mathbf{u}]$ is the jump at the discontinuity, and $\mathbf{t}_\theta$ is the traction at the discontinuity.

According to Eq. (1), the admissible displacement variations are $\delta\mathbf{u} = \delta\hat{\mathbf{u}} + \delta\tilde{\mathbf{u}}$. Moreover, from Eq. (2) it follows that $\nabla^s\delta\tilde{\mathbf{u}} = \mathbf{0}$. By successively taking: (*i*) $\delta\tilde{\mathbf{u}} = \mathbf{0}$ and (*ii*) $\delta\hat{\mathbf{u}} = \mathbf{0}$ the following system is derived:

$$\int_{\Omega\setminus\Gamma_d} (\nabla^s \delta\hat{\mathbf{u}}) : \boldsymbol{\sigma}(\hat{\boldsymbol{\varepsilon}}) d\Omega = \int_{\Omega\setminus\Gamma_d} \delta\hat{\mathbf{u}} \cdot \bar{\mathbf{b}} \, d\Omega + \int_{\Gamma_t} \delta\hat{\mathbf{u}} \cdot \bar{\mathbf{t}} \, d\Gamma \tag{8a}$$

$$\int_{\Gamma_d} \delta[\mathbf{u}] \cdot \mathbf{t}_\theta \, d\Gamma = \int_{\Omega\setminus\Gamma_d} \delta\tilde{\mathbf{u}} \cdot \bar{\mathbf{b}} \, d\Omega + \int_{\Gamma_t} \delta\tilde{\mathbf{u}} \cdot \bar{\mathbf{t}} \, d\Gamma. \tag{8b}$$

The variational Eqs. (8a) and (8b) can be generalised to a body containing multiple splitting discontinuities, by simply recalling that $\Gamma_d = \bigcup_{i=1}^{n_d} \Gamma_d^i$ (Fig. 2).

Since the traction continuity condition is enforced in the weak sense by Eq. (8b), a symmetric formulation is obtained for a symmetric traction–separation law.

2.3. Discretisation

The following equations are used to interpolate the displacement field at each finite element:

$$\mathbf{u}^e = \mathbf{N}^e(\mathbf{x})(\hat{\mathbf{a}}^e + \tilde{\mathbf{a}}^e) \quad \text{in} \quad \Omega^e \setminus \Gamma_d^e, \tag{9a}$$

$$[u]_\theta^e = w_\theta^e \quad \text{at} \quad {\Gamma_d^i}^e, \tag{9b}$$

where $(\cdot)^e$ relates $(\cdot)$ to the respective finite element, $\mathbf{N}^e$ is composed by the element shape functions, $\hat{\mathbf{a}}^e$ and $\tilde{\mathbf{a}}^e$ are, respectively, the nodal degrees of freedom associated with $\hat{\mathbf{u}}^e$ and $\tilde{\mathbf{u}}^e$, and w_θ^e is the element degree of freedom associated with each discontinuity opening.

The enhanced nodal degrees of freedom can be expressed as a function of w_θ^e:

$$\tilde{\mathbf{a}}^e = \mathbf{M}_w^{ek} w_\theta^e, \tag{10}$$

where $\mathbf{M}_w^{ek}$ is a column matrix containing $\mathbf{M}_w$, stacked in rows, evaluated at each finite element node. Therefore, this matrix is responsible for transmitting the jump at the discontinuity opening to the finite element nodes as a rigid body motion. The interpolation of the enhanced displacement field is:

$$\tilde{\mathbf{u}}^e = \mathbf{N}^e \mathbf{M}_w^{ek} w_\theta^e = \mathbf{M}_w w_\theta^e, \tag{11}$$

where $\mathbf{N}^e\mathbf{M}_w^{ek} = \mathbf{M}_w$, which is in agreement with Eq. (5).

The strain field in the bulk is approximated by means of the strain–displacement matrix $\mathbf{B}^e$:

$$\hat{\boldsymbol{\varepsilon}}^e = \mathbf{B}^e(\mathbf{x})\hat{\mathbf{a}}^e. \tag{12}$$

The incremental stress field in the bulk is:

$$d\boldsymbol{\sigma}^e = \mathbf{D}^e\mathbf{B}^e d\hat{\mathbf{a}}^e. \tag{13}$$

The traction at the discontinuity is obtained, in incremental format, as:

$$dt_\theta^e = T_{\theta\theta}^e dw_\theta^e, \tag{14}$$

where $T_{\theta\theta}^e$ is the discontinuity constitutive relation, defined according to the specific material law used. All remaining components of $\mathbf{T}^e$ are assumed to be null.

Eqs. (8a) and (8b) are discretised, by means of the previous equations, into the following system:

$$\mathbf{K}_{\hat{a}\hat{a}}^e d\hat{\mathbf{a}}^e = d\hat{\mathbf{f}}^e, \tag{15a}$$

$$K_d^e dw_\theta^e = d\tilde{f}_\theta^e, \tag{15b}$$

where:

$$\mathbf{K}^e_{\hat{a}\hat{a}} = \int_{\Omega^e \setminus \Gamma^e_d} \mathbf{B}^{e^T} \mathbf{D}^e \mathbf{B}^e \, d\Omega^e, \tag{16}$$

$$K^e_d = \int_{\Gamma^e_d} T^e_{\theta\theta} \, d\Gamma^e \tag{17}$$

and the external forces are:

$$d\hat{\mathbf{f}}^e = \int_{\Omega^e \setminus \Gamma^e_d} \mathbf{N}^{e^T} d\bar{\mathbf{b}}^e \, d\Omega^e + \int_{\Gamma^e_t} \mathbf{N}^{e^T} d\bar{\mathbf{t}}^e \, d\Gamma^e, \tag{18a}$$

$$d\tilde{f}^e_\theta = \int_{\Omega^e \setminus \Gamma^e_d} \mathbf{M}^T_w d\bar{\mathbf{b}}^e \, d\Omega^e + \int_{\Gamma^e_t} \mathbf{M}^T_w d\bar{\mathbf{t}}^e \, d\Gamma^e. \tag{18b}$$

The system of Eqs. (15a) and (15b) are uncoupled, being Eq. (15a) related to the bulk and Eq. (15b) to the discontinuities. These equations can be further developed. Replacing $\hat{\mathbf{a}}^e$ by $\mathbf{a}^e - \mathbf{M}^{ek}_w w^e_\theta$, the following system of equations is derived, where $\mathbf{a}^e$ and w^e_θ are the unknowns of the problem:

$$\mathbf{K}^e_{\hat{a}\hat{a}} d\mathbf{a}^e - \mathbf{K}^e_{aw} dw^e_\theta = d\hat{\mathbf{f}}^e, \tag{19a}$$

$$-\mathbf{K}^e_{wa} d\mathbf{a}^e + \left(K^e_d + \mathbf{M}^{ek^T}_w \mathbf{K}^e_{\hat{a}\hat{a}} \mathbf{M}^{ek}_w\right) dw^e_\theta = -\mathbf{M}^{ek^T}_w d\hat{\mathbf{f}}^e + d\tilde{f}^e_\theta, \tag{19b}$$

where:

$$\mathbf{K}^e_{aw} = \mathbf{K}^e_{\hat{a}\hat{a}} \mathbf{M}^{ek}_w \tag{20}$$

and

$$\mathbf{K}^e_{wa} = \mathbf{K}^{e\ T}_{aw}. \tag{21}$$

Recalling that $\mathbf{N}^e \mathbf{M}^{ek}_w = \mathbf{M}_w$, it is possible to verify that: $-\mathbf{M}^{ek^T}_w d\hat{\mathbf{f}}^e + d\tilde{f}^e_\theta = 0$.

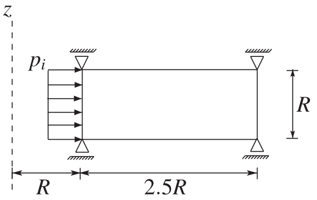

Fig. 4. Structural scheme.

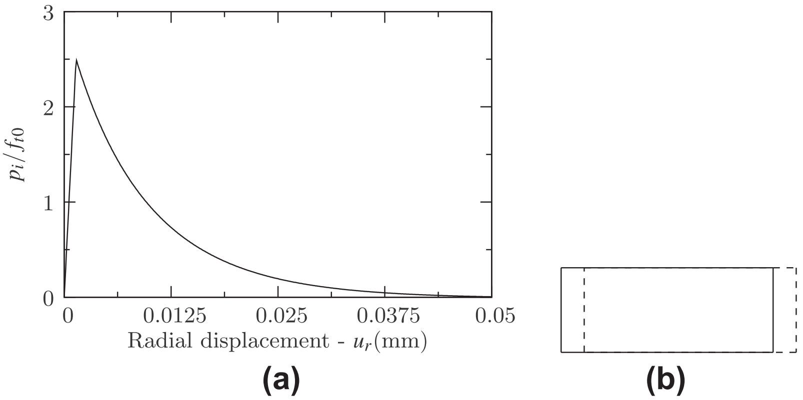

Fig. 5. Results with one finite element: (a) radial displacement vs. relative inner pressure; and (b) deformed mesh (displacements amplified 10 times) for $u_r = 0.1$ mm.

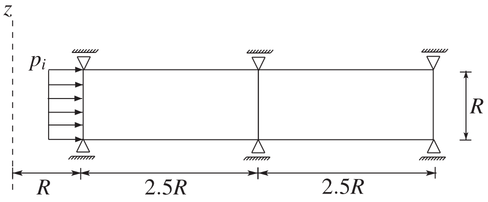

Fig. 6. Structural scheme.

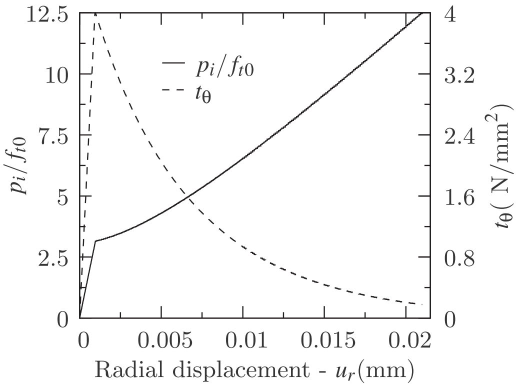

Fig. 7. Radial displacement vs. relative inner pressure and traction for two finite elements.

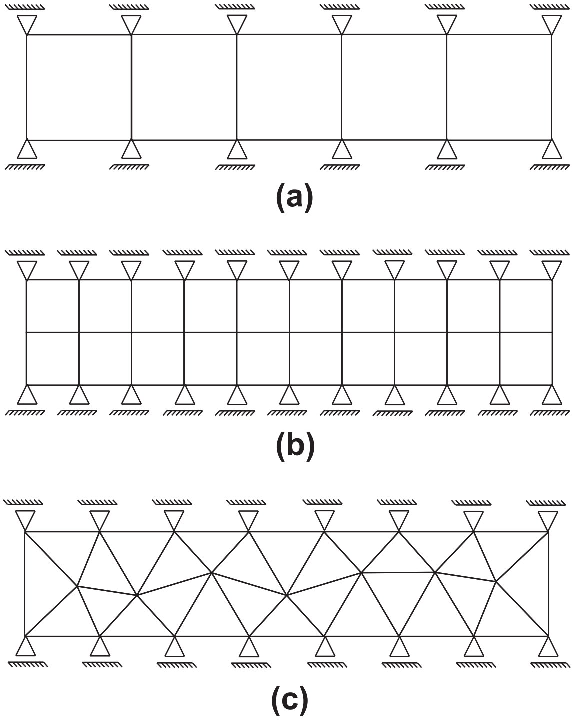

Fig. 8. Adopted mesh with: (a) *5*; (b) *20* bilinear finite elements; and (c) *28* linear finite elements.

3. Implementation

Each discontinuity must always cross an entire parent element. An embedded discontinuity is inserted whenever σ_θ, evaluated at the centroid of the parent element, reaches the tensile strength of the material. At this stage, new degrees of freedom are added, one per finite element, allowing the tractions to be controlled by the traction–separation law. Since a constant jump is considered at each enriched parent element, the continuity of jumps across boundaries cannot be imposed. Therefore, the additional degrees of freedom are internal to the element and a condensation is performed to keep the bandwidth of the global stiffness matrix unchanged by the progressive enrichment of parent elements. A similar procedure has been adopted in other embedded approaches [12–18].

Eq. (19b) is solved for dw_θ^e giving:

$$dw_\theta^e = \left(K_d^e + \mathbf{M}_w^{ek^T}\mathbf{K}_{\hat{a}\hat{a}}^e\mathbf{M}_w^{ek}\right)^{-1}\mathbf{K}_{wa}^e d\mathbf{a}^e, \tag{22}$$

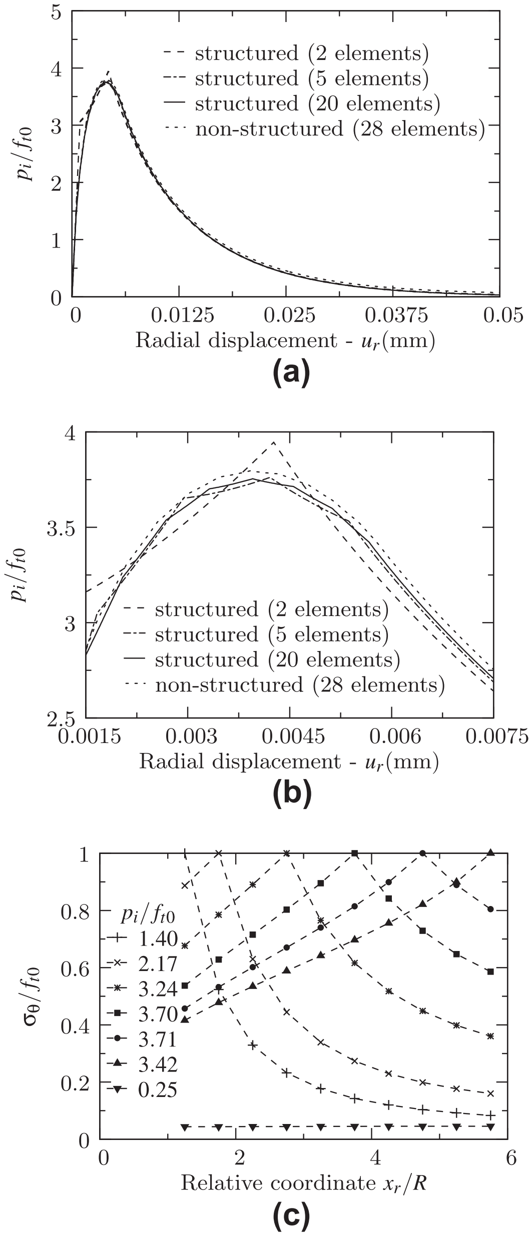

Fig. 9. Mesh discretisation results: (a) radial displacement vs. relative inner pressure for different mesh discretisation; (a) detail of the radial displacement vs. relative inner pressure curve for different mesh discretisation; and (c) relative hoop stress for different values of relative inner pressure along the *r*-axis for 20 finite elements.

and dw^e_θ is substituted in Eq. (19a):

$$\underbrace{\left[\mathbf{K}^e_{\hat{a}\hat{a}} - \mathbf{K}^e_{aw}\left(K^e_d + \mathbf{M}^{ek^T}_w \mathbf{K}^e_{\hat{a}\hat{a}} \mathbf{M}^{ek}_w\right)^{-1} \mathbf{K}^e_{wa}\right]}_{\mathbf{K}^e_{con}} d\mathbf{a}^e = d\hat{\mathbf{f}}^e, \tag{23}$$

leading to:

$$\mathbf{K}^e_{con} d\mathbf{a}^e = d\hat{\mathbf{f}}^e. \tag{24}$$

4. Traction–separation law

The bulk is assumed linear elastic. The traction–separation material law is taken from the damage theory and all physical parameters, such as fracture energy, concern to mode-I of fracture [6].

The following traction–separation law is adopted:

$$t_\theta = (1 - d)k_\theta w_\theta, \tag{25}$$

where d is a scalar damage variable ($0 \leqslant d \leqslant 1$) and k_θ is a linear elastic penalty that avoids overlapping of crack faces under closure.

Two damage functions are adopted; (*i*) an exponential one:

$$d = d(\kappa) = 1 - \frac{f_{t0}}{k_\theta w_\theta} \exp\left(-\frac{f_{t0}}{G_F}\kappa\right) \tag{26}$$

and (*ii*) a linear function:

$$d = d(\kappa) = \begin{cases} 1 - \frac{f_{t0}}{k_\theta w_\theta}\left(1 - \frac{f_{t0}}{2G_F}\kappa\right) & \text{if } \kappa < 2\frac{G_F}{f_{t0}} \\ 1 & \text{otherwise} \end{cases}, \tag{27}$$

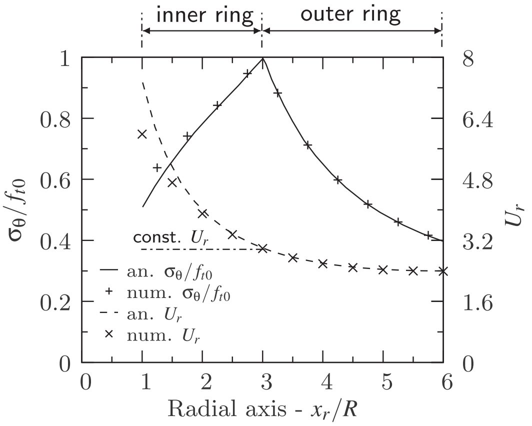

Fig. 10. Relative hoop stress and relative radial displacement along *r*–axis for numerical and analytical model by Nielsen and Bićanić [2].

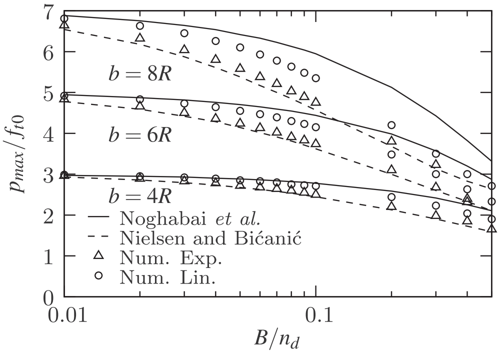

Fig. 11. Relative maximum inner pressure vs. *B*/*d* for outer radius equal to 4*R*, 6*R* and 8*R*.

where κ is a scalar variable defined by:

$$\kappa = \max\langle w_\theta\rangle^+, \kappa \geqslant 0, \dot{\kappa} \geqslant 0, \tag{28}$$

f_{t0} is the tensile strength and G_F is the fracture energy of the material. In fact, the tensile strength should correspond to the biaxial condition of tension–compression due to the compressive radial stress [2]. For the sake of simplicity, the tensile strength of the material is assumed.

A loading function is given in the jump space:

$$f = w_\theta - \kappa. \tag{29}$$

Each discontinuity opens when the hoop stress σ_θ reaches f_{t0}. The damage law should be chosen according to the problem at hand [6].

5. Small examples

In this section some small academic examples are computed in order to better assess the capacity of full softening the applied load and the mesh independence of the present formulation.

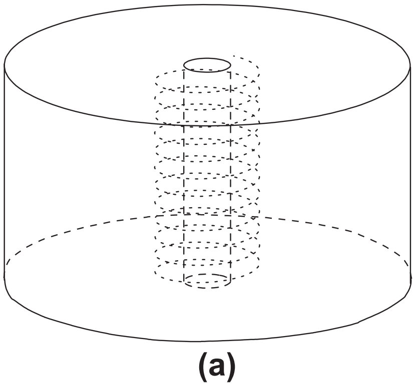

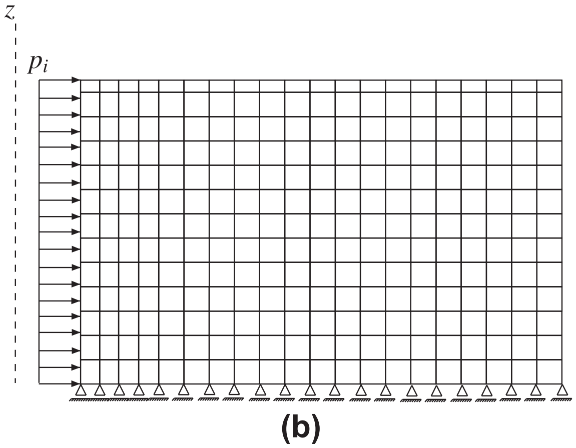

Fig. 12. (a) scheme of the specimens adopted by Noghabai [4] and (b) mesh chosen to simulate the experimental tests.

Table 1
Material parameters for NSC, HSC, and VHSC.

	NSC	HSC	VHSC
f_{c0} (N/mm^2)	57.0	105.0	157.4
f_{t0} (N/mm^2)	3.8	5.0	8.0
G_f (N/mm)	0.105	0.145	0.172
E_c (N/mm^2)	33,800	39,400	41,200

The arc-length procedure is adopted in the numerical solution by enforcing a monotonic increase of the crack opening.

5.1. Single finite element

Consider the finite element represented in Fig. 4, where $R = 3.7$ mm.

The material parameters are the following: Young's modulus $E = 15{,}000$ N/mm^2; Poisson's ratio $\nu = 0$; tensile strength $f_{t0} = 4.0$ N/mm^2; fracture energy $G_F = 0.125$ N/mm and the hoop penalty $k_\theta = 10^{10}$ N/mm^3. When the opening criterion is reached, the negative exponential softening law given from Section 4 is applied with $n_d = 2$.

The radial displacement (for the upper left node), u_r, vs. relative inner pressure, p_i/f_{t0}, is represented in Fig. 5a, whereas the deformed mesh is depicted in Fig. 5b for a radial displacement equal to 0.1 mm.

Note that full softening of the applied pressure is achieved and no stress locking is obtained. The contribution of the linear elastic deformation of the bulk to the total radial displacement is negligible (Fig. 5a). Therefore, the deformed mesh consists almost exclusively of a rigid body translation along the r-axis due to the opening of the discontinuity (Fig. 5b).

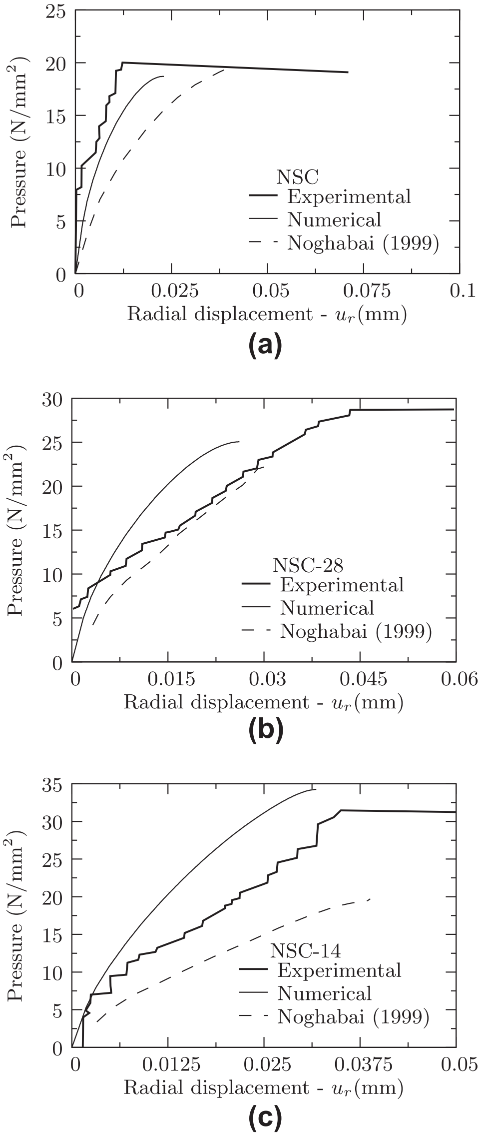

Fig. 13. NSC results: (a) reference specimen; (b) specimen with spiral reinforcement with 28 mm pitch; and (c) specimen with spiral reinforcement with 14 mm pitch.

5.2. Combined finite elements

A similar example is computed considering an additional finite element, which is not allowed to crack (see Fig. 6).

In Fig. 7, the radial displacement vs. relative inner pressure and the radial displacement vs. hoop stress, t_θ are shown. The latter is depicted by evaluating the hoop stress at centroid of the first finite element until f_{t0} is reached. Immediately afterwards, the discontinuity is inserted and the hoop stress is given by the discontinuity traction.

Regarding the radial displacement vs. relative inner pressure curve, a sudden change of stiffness is obtained when the discontinuity is activated ($t_\theta = f_{t0}$). From this point onwards, the tangent stiffness of the first element gradually decreases towards zero. The external finite element confines the internal one leading to an increasing inner pressure.

5.3. Mesh discretisation

The example given in Section 5.1 is now used to assess the role of discretisation and regularity of the mesh. A total of four meshes are computed: (*i*) three structured meshes containing respectively 2, 5, and 20 bilinear finite elements (Figs. 6, 8a and b) and (*ii*) a non-structured mesh containing 28 linear finite elements (Fig. 8c). All finite elements are progressively enriched when the initiation criterion is fulfilled (Section 3).

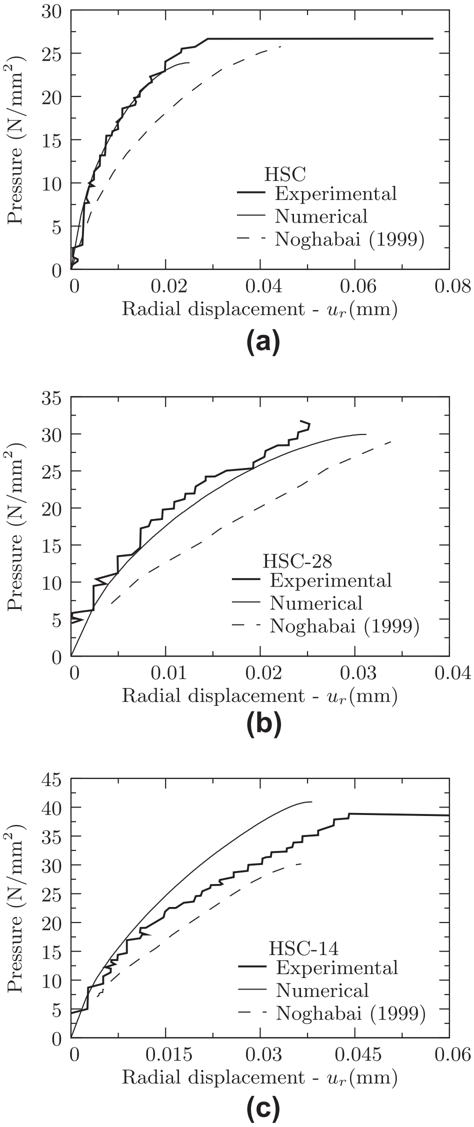

Fig. 14. HSC results: (a) reference specimen; (b) specimen with spiral reinforcement with 28 mm pitch; and (c) specimen with spiral reinforcement with 14 mm pitch.

The radial displacement vs. relative inner pressure curves are depicted in Fig. 9a. From this figure it can be concluded that the overall softening behaviour is accurately described in all meshes. However, a zoom near the peak load represented in Fig. 9b shows that the coarser meshes overestimate the peak load. In Fig. 9c, the relative hoop stress at the centroid of each finite element, along r-axis, is represented. Immediately before any discontinuity is inserted, for $p_i/f_{t0} = 1.40$, the hoop stress matches the linear elastic solution. Afterwards, whenever the tensile strength is reached at the centroid of a finite element, a discontinuity is inserted undergoing softening. Several curves corresponding to different inner pressures are also represented.

6. Comparison with analytical formulations

The results obtained with the mesh presented in Fig. 8b, which corresponds to the structural scheme of Fig. 6, are compared to analytical solutions obtained by Nielsen and Bićanić [2] and Noghabai [4]. These authors developed analytical models to describe radial cracking around a ribbed reinforcement assuming some simplifying hypotheses: Nielsen and Bićanić [2] considered the radial displacements in the inner cracked ring to follow the linear elastic distribution and subsequently applied an exponential softening law to describe the hoop stress evolution; Noghabai [4] assumed constant radial displacements inside the inner cracked ring and adopted a linear softening law.

First, the radial displacements distribution is addressed. The material properties of previous examples are adopted herein. According to the work presented in Nielsen and Bićanić [2], the following parameter B can be computed, which, together with the number of discontinuities n_d, is related to the brittleness of the material:

$$B = \frac{2\pi R}{l_{ch}} \approx 0.20, \qquad l_{ch} = \frac{EG_F}{f_{t0}^2} \approx 117\ \text{mm} \tag{30}$$

and $B/n_d \approx 0.10$.

In Fig. 10 the evolution along r-axis of relative hoop stress with a normalised radial displacement, $U_r = u_r/(R\,f_{t0}/E)$, is shown when the discontinuity front reaches $x_r = 3R$. Differences are only found near $x_r = R$, where the numerical relative radial displacement field is smaller than the assumed elastic shape of the analytical model. Note that the numerical result for U_r, inside the inner ring, lies between the linear elastic distribution and the constant value adopted by Noghabai [4].

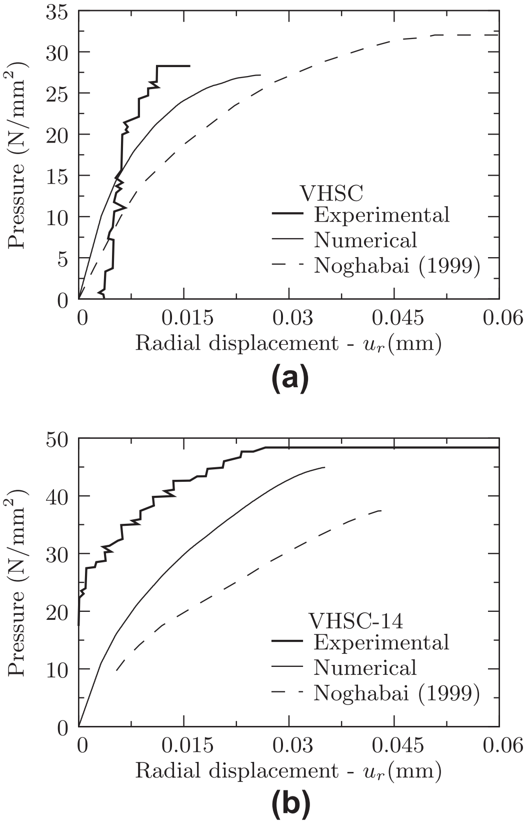

Fig. 15. VHSC results: (a) reference specimen; and (b) specimen with spiral reinforcement with 14 mm pitch.

The structural scheme in Fig. 6 has an outer radius of 6*R*. This model is rerun with both linear and exponential constitutive models from Section 4, for different brittleness numbers, ranging from $B/n_d = 0.01$ to $B/n_d = 0.5$, corresponding to different values of G_F. Two additional meshes with outer radius equal to 4*R* and 8*R* are also computed.

The relative maximum inner pressure obtained is represented in Fig. 11 using analytical results from Noghabai [4] and Nielsen and Bićanić [2]. The numerical results are between both analytical results, although closer to those obtained by Nielsen and Bićanić [2]. This is certainly related to the fact that the distribution of radial displacements obtained numerically (Fig. 10) is closer to the distribution assumed by Nielsen and Bićanić [2] than the constant displacement field adopted by Noghabai [4].

7. Simulation of experimental tests

Noghabai [4] carried out experimental work concerning concrete cylinders subjected to increasing inner pressure. The geometry of the specimen is schematically represented in Fig. 12a. The outer diameter is 313 mm, the concentric drilled hole diameter is 36 mm and the depth of the specimen is 175 mm.

Three concrete mixtures have been considered: (*i*) a normal-strength concrete (NSC); (*ii*) a high-strength concrete (HSC); and (*iii*) a very-high-strength concrete (VHSC). The material properties are listed in Table 1. For each mixture, a plain specimen is used as reference. Two additional specimens containing a spiral reinforcement with a diameter of 81.0 mm and, respectively, 28 mm and 14 mm pitches have been produced. The cross section of the reinforcement is 6 mm, whereas the tensile strength is $f_{sy} = 380\ \mathrm{N/mm^2}$.

A numerical simulation of the previously described specimens with: (*i*) a discrete; (*ii*) a smeared; and (*iii*) an inner softening band approach has been performed in [6]. However, a ring model has been used to simulate the evolution of the number of active radial cracks. Noghabai [6] concludes that the discrete crack approach using a linear softening model

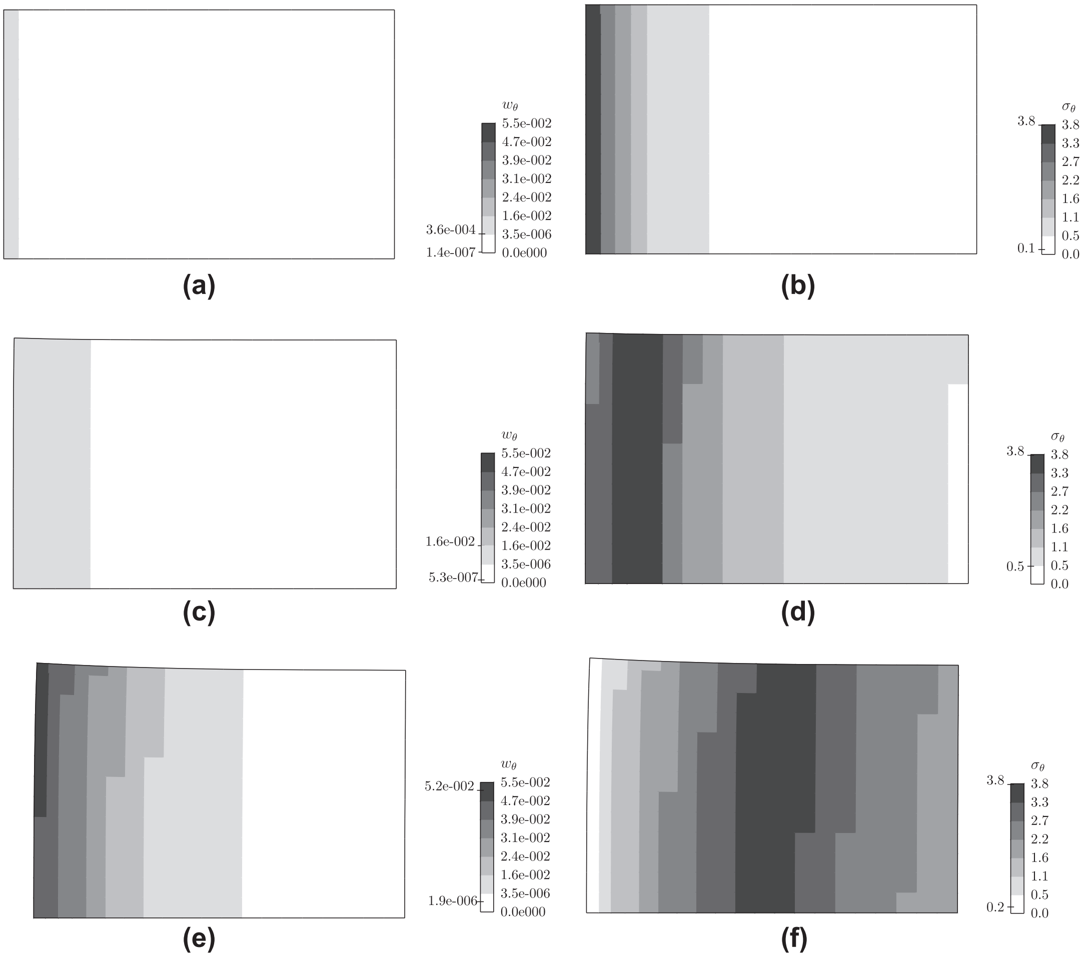

Fig. 16. Numerical results for the NSC reference specimen (displacements amplified 500 times): (a), (c), and (e) crack opening; (b), (d), and (f) traction, for respectively $u_r = 0.20 \times 10^{-2}$, $u_r = 0.80 \times 10^{-2}$, and $u_r = 0.23 \times 10^{-1}$.

approximates the peak load better in relation to an exponential softening model. Therefore, the formulation presented in Section 2, which is developed within the scope of the discrete crack approach, is applied with a linear softening model. The material parameters are listed in Table 1. Furthermore, since it is experimentally observed that the number of active discontinuities is relatively stable, an average number $n_d = 3$ is assumed for all specimens.

The adopted mesh is composed by 260 axisymmetric bilinear finite elements representing the bulk (Fig. 12b) and axisymmetric point elements to simulate the spiral reinforcement. The latter is placed at a radius of 40.5 mm along the height of the specimen. Loading is controlled using the arc-length method to enforce the monotonic increase of the opening of the first cracked finite element.

Figs. 13–15 contain respectively, the results obtained for the NSC, HSC, and VHSC specimens. It is emphasised that there are no experimental results concerning the VHSC specimen with spiral reinforcement with 28 mm pitch. All represented charts include the present numerical analysis, the inner pressure vs. radial displacement curves from the experimental data [4] and the numerical results obtained by Noghabai [6] with a discrete crack approach applied to a ring model with a linear softening law. Experimentally, the radial displacement was measured by averaging two orthogonal directions symmetrically placed over the hole, at radius of 29 mm. Numerically, the radial displacement is directly provided from the horizontal displacement of the upper node of the mesh, which is placed at the referred radius.

In Fig. 16, the crack opening pattern and corresponding hoop stress for different stages of loading are shown. The crack front is defined by the elements reaching the tensile strength of the material. This front gradually evolves from the top of the specimen to the bottom along the same vertical line. Additionally, it is observed that the crack front propagates along the r-axis at the same time the stresses are gradually released closer to the symmetry axis. It is emphasised that the existing ring models cannot simulate the distribution of radial cracks along the specimen axis.

8. Summary and conclusions

In this paper, a new axisymmetric formulation capable of simulating radial splitting fracture is presented. With this approach a discrete strong discontinuity is embedded into finite elements as if it were an interface element. Consequently mesh independence is obtained. The corresponding hoop jumps, which are assumed constant inside each finite element, are then transferred by means of a rigid body motion. Under this hypothesis, the stresses in the continuum are only due to the regular part of the strain field. Traction continuity is enforced in a weak sense; as a consequence, symmetry is kept if a symmetric constitutive traction–separation law is provided. In addition, fully advantage of static condensation is considered, keeping constant the number of degrees of freedom and the bandwidth of the stiffness matrix.

In all computed examples, complete softening of the applied inner pressure is achieved and no stress locking is found. Relatively coarse meshes can be used to adequately capture the global response. A good agreement was found with the analytical results presented in [2,4].

From the simulation of experimental tests presented in Noghabai [4], a good accuracy is observed for all specimens with three different concrete mixtures, including both plain and reinforced situations. Furthermore, conversely to the other approaches, the proposed model allows to simulate the propagation of the radial cracks along the axis of the specimen.

References

[1] Tepfers R. Cracking of concrete cover along anchored deformed reinforcing bars. Mag Conc Res 1979;31(106):3–12. doi:10.1680/macr.1979.31. 106.3.
[2] Nielsen CV, Bićanić N. Radial fictitious cracking of thick-walled cylinder due to bar pull-out. Mag Conc Res 2002;54(3):215–21. doi:10.1680/macr.54.3.215.38797.
[3] Reinhardt H, van der Veen C. Splitting failure of a strain-softening material due to bond stresses. In: Carpinteri A, editor. Applications of fracture mechanics to reinforced concrete. Amsterdam: The Netherlands; 1992. p. 333–46.
[4] Noghabai K. Effect of tension softening on the performance of concrete structures. Experimental, analytical and computational studies. Ph.D. thesis, Luleå University of Technology; 1998.
[5] Bažant ZP, Planas J. Fracture and size effect in concrete and other quasibrittle materials. CRC Press; 1997.
[6] Noghabai K. Discrete versus smeared versus element-embedded crack models on ring problem. J Engng Mech 1999;125(3):307–15. http://dx.doi.org/10.1061/(ASCE)0733-9399(1999)125:3(307).
[7] Cox JV, Herrmann LR. Validation of a plasticity bond model for steel reinforcement. Mech Cohes-Frict Mat 1999;4(4):361–89.
[8] Gálvez JC, Benítez JM, Tork B, Casati MJ, Cendón DA. Splitting failure of precast prestressed concrete during the release of the prestressing force. Engng Fail Anal 2009;16(8):2618–34. doi:10.1016/j.engfailanal.2009.04.023.
[9] Hillerborg A, Modeer M, Petersson PE. Analysis of crack formation and crack growth in concrete by means of fracture mechanics and finite elements. Cem Conc Res 1976;6(6):773–81. doi:10.1016/0008-88476)90007-7.
[10] Dias-da-Costa D, Alfaiate J, Sluys LJ, Júlio ENBS. A discrete strong discontinuity approach. Engng Fract Mech 2009;76(9):1176–201. doi:10.1016/j.engfracmech.2009.01.011.
[11] Malvern LE. Introduction to the mechanics of a continuous medium. Englewood Cliffs (NJ): Prentice-Hall International; 1969.
[12] Dvorkin EN, Cuitiño AM, Gioia G. Finite elements with displacement interpolated embedded localization lines insensitive to mesh size and distortions. Int J Numer Methods Engng 1990;30(3):541–64. doi:10.1002/nme.1620300311.
[13] Klisinski M, Runesson K, Sture S. Finite element with inner softening band. J Engng Mech 1991;117(3):575–87. http://dx.doi.org/10.1061/(ASCE)0733-9399(1991)117:3(575).
[14] Simo JC, Oliver J, Armero F. An analysis of strong discontinuities induced by strain-softening in rate-independent inelastic solids. Comput Mech 1993;12(5):277–96. doi:10.1007/BF00372173.
[15] Armero F, Garikipati K. An analysis of strong discontinuities in multiplicative finite strain plasticity and their relation with the numerical simulation of strain localization in solids. Int J Solids Struct 1996;33(20–22):2863–85. doi:10.1016/0020-768(95)00257-X.
[16] Oliver J. Modelling strong discontinuities in solid mechanics via strain softening constitutive equations. part 1: Fundamentals. Int J Numer Methods Engng 1996;39(21):3575–600.

[17] Oliver J. Modelling strong discontinuities in solid mechanics via strain softening constitutive equations. Part 2: Numerical simulation. Int J Numer Methods Engng 1996;39(21):3601–23.

[18] Linder C, Armero F. Finite elements with embedded strong discontinuities for the modeling of failure in solids. Int J Numer Methods Engng 2007;72(12):1391–433. doi:10.1002/nme.2042.